An analytical model of the dynamic response of UHMWPE laminated plate to ballistic impact

Huiru Jia[1], Yongxi Jin[4], Tan PJ[5], Ye Yuan[1,2,3*]

[1]*State Key Laboratory of Explosion Science and Safety Protection, Beijing Institute of Technology, Beijing 100081, PR China*

[2]*Chongqing Innovation Center, Beijing Institute of Technology, Chongqing 401120, PR China*

[3]*China Safety Technology Research Academy of Ordnance Industry, Beijing 100053, PR China*

[4] *Zhiyuan Research Institute, Hangzhou, PR China*

[5] *Department of Mechanical Engineering, University College London, London, UK*

Abstract

This paper develops an analytical model for the ballistic impact response of UMHWPE laminated plate, which is capable of capturing transient transverse bulging deformation and flexural wave propagation. The mathematical framework of the analytical model is based on the is based on first-order shear deformation plate theory, which uses damage mechanics to model the progressive through-thickness fracture of the laminated plate. Compared to existing analytical models, the current model does not need to make assumptions for the travelling hinge speed which is solved via modal analysis and Lagrangian equation. Analytical predictions of transverse bulging deflection, travelling hinge position and ballistic limit velocity are validated against experimental data reported in the literature and they will be shown to be in good agreement for varying projectile sizes and laminate thicknesses. The maximum equivalent stress of the impact-receiving layer is found to be governed by the travelling hinge's position, which can be alleviated with the expansion of the bulging deformation area. At an impact velocity above the ballistic limit, the energy dissipated through transverse shear in the local penetration phase is significantly higher than in the subsequent bulging deformation phase.

Keywords: UMHWPE laminated plate; Analytical model; Ballistic limit velocity; Transverse bulging deflection; Travelling hinge

*Corresponding author

Email address: yuanye20@bit.edu.cn (Ye Yuan[1,2,3])

1. Introduction

Ultra-high molecular weight polyethylene (UHMWPE) laminated plates have been increasingly employed in armour systems, due to superior mechanical performance such as high specific strength

Nomenclature

a	Half length of the laminated plate
A_{ij}	Extensional stiffness
A_p	Cross-sectional area of the projectile
C_t	Transverse wave speed
D_1, D_2	Damage parameters
D_{ij}	Bending stiffness
E_1, E_2, E_3	Young's modulus
G_{12}, G_{23}	Shear modulus
h	Intact thickness
h_0	Total thickness
h_1	Perforated thickness in phase I
h_2	Remaining thickness at the beginning of phase II
h_L	Thickness of each layer
K	Shear correction factor
$\mathcal{L}$	*Lagrangian*
m_p	Projectile mass
M	Bending moment
N	Membrane force
Q	Shear force
Q_{ij}	Plane stress-reduced stiffness components
R	Projectile radius
t	Time
t_1	Time duration in phase I
t_f	Time instant when the motion of projectile ceases or full penetration occurs
$t' = t - t_1$	Passage of time in phase II
$v = \dot{w}_0(t)$	Projectile's velocity
v_i	Initial velocity of the projectile
v_r	Residual velocity of the projectile
v_{bl}	Ballistic limit velocity
w_0	Transverse central bulging deflection
$\gamma_{xz0}, \gamma_{yz0}$	Shear displacements
ϵ_f	Failure strain
$\epsilon_{ij}, \gamma_{ij}$	Strain components
$\epsilon^0_{ij}, \epsilon^1_{ij}$	Membrane and bending strains
ϵ_x	Tensile strain

ζ	Position of the travelling hinge
λ	Membrane effect coefficient
μ	Areal density the laminated plate
ν_{12}	Poisson's ratio
Π	Total strain energy
ρ	Density the laminated plate
σ_f	Failure stress
σ_{ij}	Stress components
$\sigma_{\max}$	Maximum equivalent stress

and specific modulus with exceptionally high wave speeds, allowing for rapid energy absorption and dispersion [1]. The cross-ply UMHWPE is a typical laminated plate, constructed from a high-volume fraction of UHMWPE fibre composites (>80%) with a [0°/90°] cross-ply architecture, and a low-volume fraction of thermoplastic polymer matrix (<20%), endowing excellent ballistic resistance to high-speed localised impact [2]. In order to assess the consequence of the ballistic impact or to achieve an optimised structural design, significant effort has been devoted to fostering an understanding of the deformation and failure mechanisms of cross-ply UHMWPE laminated plates under ballistic perforation. Transverse bulging deflection (TBD) at the non-impact-receiving face (when the integrity of the laminated plates is not compromised) and the ballistic limit velocity v_{bl} (above which the target is fully penetrated) are two important resultant effects, which attribute, respectively, to the blunt trauma injury [3, 4] on the possible substrate occupant and overall ballistic resistance performance [5, 6]. Although numerical models [7–10] exist that can provide high-fidelity solutions of the ballistic response of the cross-ply UMHWPE laminated plate, they are, in general, computationally expensive and are not feasible for large-scale iterative simulation in optimisation. This highlights the importance of developing an analytical model that permits quick and accurate estimation of the TBD and the v_{bl} while capturing the various failure modes of the cross-ply UMHWPE laminated plate at a wide range of impact velocities.

A considerable body of experimental work on the ballistic response of UMHWPE laminated plate already exists [11–16]. One example is the experiment by Nguyen et al. [17] where it was shown that the deformation and failure of UMHWPE laminated plate under ballistic impact can be delineated into three sequential stages: stage I - shear plugging in the vicinity of the impact zone with negligible TBD; stage II - delamination, matrix cracks, progressive through-thickness tearing of the fibre with large TBD; stage III - further deformation of the intact laminated plate until full penetration occurs. The progressive failure mechanisms during the aforesaid response stages are quite complex and are found to be influenced by various factors such as impact velocity [18], plate thickness [19], projectile shape [20] etc.

The response of composite laminates to localised transverse impact leads to bulging deformation dictated by the propagation of longitudinal, shear and flexural waves travelling in the composite [21]. The region of non-zero transverse bulging deformation was governed by the 'travelling hinge' (or known as the dynamic cone), which emanates from the target's centre towards the pe-

riphery [22]. Several experimental works [16, 23] studied the evolution of the lateral deformation contour using high-speed camera and 3D-DIC techniques, and highlighted the importance of the deformation pattern and the travelling hinge speed on the bulging deformation of the composite laminates. Karthikeyan et al. [19] employed the dynamic shadow moiré method to acquire back deformation data of UHMWPE laminated plates subjected to steel ball impact. They found that the lateral deformation is in a diamond shape, which expands at an approximately constant speed from the impact location until reaching the fixed boundaries. Zhu et al. [24] utilized 3D-DIC technology to observe the impact response of UHMWPE orthogonal laminated plates subjected to large-sized lead-core pistol projectile impacts. They noted that the convex deformation contour transformed from the initial diamond shape to a circular or square shape when the hinge speed along the ±45° and ±135° directions gradually exceeded that along the fibre direction. Similar phenomena were also observed by Vargas-Gonzalez et al. [4] who studied the ballistic performance of large-sized Spectra Shield laminated plates. Zhang et al. [25] employed 3D-DIC technology to capture the evolution of the bulging deformation area of Dyneema® HB80 laminated plates subjected to projectile impacts and discovered that as the tensile wave propagated through the fibres to the edges and reflected, the speed of lateral deformation decreased when reducing the initial impact velocity.

Different analytical models – based on either momentum [22, 26, 27] or energy conservation [28–30] – were developed to predict the temporal evolution of the TBD and the ballistic limit velocity of the UMHWPE laminated plate under ballistic impact. Based on an energy conservation approach, Li et al. [29] developed an analytical model to predict the time histories of the acceleration according to the energy absorbed by each through-thickness failure mode (including matrix crush, laminate shear, laminate compressive, fiber stretch, fiber break and delamination), as well as the ballistic limit velocity. The equation of motion is one-dimensional (in the out-of-plane direction) and did not consider the evolution of the lateral deformation (i.e. the travelling hinge phenomenon). Langston [30] proposed an analytical model to estimate the reduction of a projectile's kinetic energy by balancing it with the various energy absorption mechanisms activated in the composite (fiber tensile strain, delamination, matrix cracking, acceleration of the composite mass, and shear failure of the composite). As opposed to the approach in [29], the effect of the radius of wave propagation on the energy absorbed by tensile strain was considered. It was found that majority of the energy was dissipated by tensile strain and the acceleration of composite mass. Zhang et al. [27] developed an analytical model based on the conservation of momentum to predict the two-phase impact response (a local failure phase followed by a bulging deformation phase with progressive penetration of projectile) of UMHWPE laminated plate and its ballistic impact velocity. The lateral deformation was considered based on the assumption that the angle of the bulging cone is proportional to the cubic root of the initial velocity at the outset of the bulging deformation phase. Focusing on the low-speed impact case where only large deformation of the UMHWPE laminated plate is of interest, Yang et al. [22] also used conservation of momentum to derive the equation of motion for the UMHWPE laminated plate. The hinge speed was assumed to be a constant and was obtained via numerical simulation. As mentioned above, the fidelity of the analytical model relies upon the accurate prediction of the hinge speed which governs the lateral deformation region where various failure modes take place. In the above analytical models, however, the hinge speed was either approximated using or was obtained as a fixed constant

via numerical simulation, which cannot reflect the deformation mechanism due to the outward travelling stress wave as observed in the past experiments.

The objective of this work is to develop an analytical model capable of providing, in a computational efficient way, accurate prediction of deformation (both lateral and transverse) and failure associated with the dynamic elastic response of a UMHWPE laminated plate subjected to ballistic impact. Modal analysis and Lagrangian equation – which were frequently used to deal with the nonlinear response of metallic [31] and laminated [32, 33] plates involving complex behaviours such as large deformation, flexural wave propagation, and fracture – will be used to derive the governing equations to obtain the transient TBD and hinge velocity of the UMHWPE laminated plate. Damage criteria, based on critical stress and strain, are incorporated to capture the progressive fracture. Predictions by the analytical model are validated against existing experimental data. Insights into the dynamic deformation and failure response of the UMHWPE laminated plate were revealed through the analytical predictions. A parametric study is carried out to investigate the influence of impact velocity on the ballistic response of the laminated plate.

2. Modal formulation

This section presents the development of an analytical model which permits quick estimation of transient bulging deflection and failure of a fully clamped UHMWPE laminated plate subjected to ballistic impact. The key features of the proposed analytical model are as follows: (1) a ballistic model was used to simulate the local penetration phase of the UHMWPE laminated plate; (2) the first-order shear deformation plate theory is used to model the deformation phase of the laminated plate; (3) the region of non-zero deformation was dictated by the travelling hinge due to flexural wave propagation; (4) governing equations of deformation and hinge speed were derived based on modal analysis; (5) damage criteria were introduced to predict the progressive failure of sub-laminates in the out-of-plane direction. The prediction will be validated against existing experimental data in Section 3.

2.1. Problem statement and modeling approach

Consider a fully clamped square UHMWPE laminated plate subjected to the normal impact of a rigid blunt projectile with an initial velocity of v_i as depicted in Fig. 1. The composite square plate has a length of $2a$ and an initial thickness of h_0. The projectile has mass m_p and a diameter of $2R$. The UMHWPE laminated plate was made of a stack of [0°/90°] orthogonal plies. To eliminate the influence of ply orientation on the stiffness matrix computation, the laminated plate was discretised into a stack of homogenous layers. Each layer consisted of four plies in a [0°/90°/0°/90°] lay-up with a sub-laminate thickness of h_L. This homogenisation approach follows the same used in [27] to allow failure to occur progressively in each sub-laminate.

The penetration of the projectile into the target consists of two consecutive phases: phase I - local penetration with no deformation and phase II - global deformation with progressive damage, as shown in Fig. 2. For simplicity, it shall be assumed that response phases I and II are uncoupled. In phase I, the projectile's velocity was estimated based on the contact stress (resulted from stress wave propagation and reflection) exerted on the target. Phase I ends when the compression wave

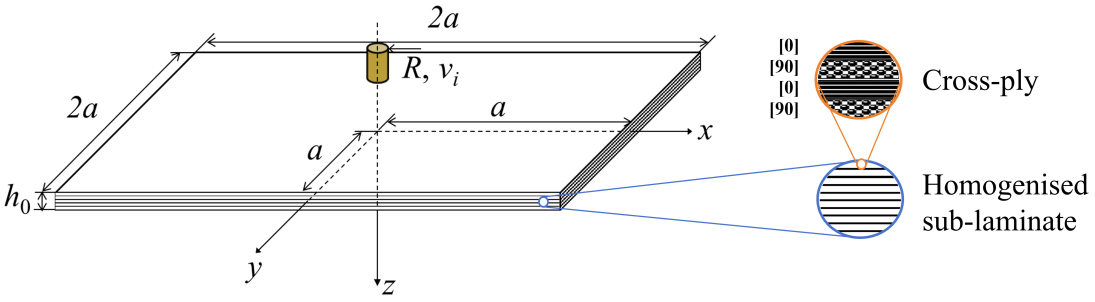

Figure 1: Schematic of UMHWPE laminated plate subjected to impact by a rigid blunt projectile.

in the penetration zone encounters the tension wave reflected from the back layer of the laminated plate [34]. The penetration depth in phase I is denoted as h_1. The remaining intact laminated plate with a thickness of $h_2 = h_0 - h_1$ subsequently undergoes dynamic bulging deformation. The deformation of the laminated plate in phase II was governed by the propagation of flexural waves. The intact sub-laminate that resists the projectile gradually diminishes due to progressive penetration across the thickness. We employed a similar approach to that of Yuan et al. [32, 33] to derive the equation of motion in the form of ODEs. A critical equivalent stress and strain criteria were used to capture the progressive failure. Various assumptions concerning laminated plate deformation and failure criteria will be detailed in the following subsections.

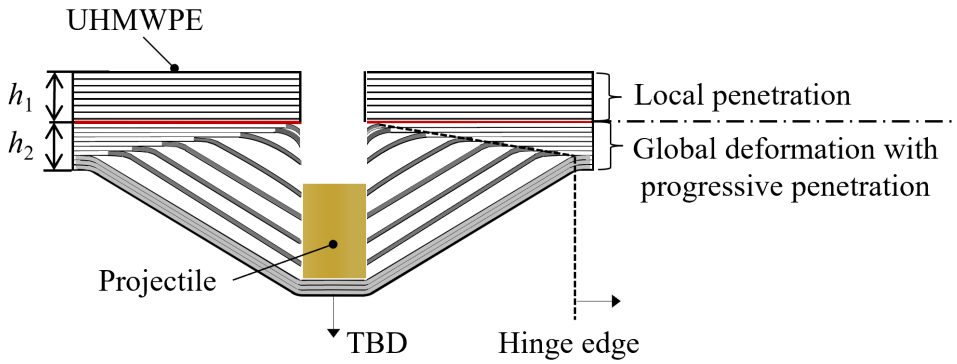

Figure 2: Schematic of two-phase penetration model for UMHWPE laminated plate.

2.2. *Phase I response (local penetration):* $0 < t \leq t_1$

Upon projectile impact as shown in Fig. 3, a compressive stress wave is generated in the laminated plate, propagating through its thickness at a transverse velocity C_t, given as

$$C_t = \sqrt{\frac{E_3}{\rho}} \tag{1}$$

where E_3 and ρ are the transverse elastic modulus and density of the composite. The compressive stress wave can be treated as one-dimensional (1D). The contact stress was related to the

projectile's velocity during phase I:

$$\sigma = \frac{M_p}{A_p}\frac{\mathrm{d}v}{\mathrm{d}t} = -\rho C_t v \tag{2}$$

where v is the projectile velocity at time t, and A_p is the cross-sectional area of the projectile. The projectile velocity v was solved from Eq. 2 which is written in the following form:

$$v = v_i e^{-\rho C_t A_p t/m_p}. \tag{3}$$

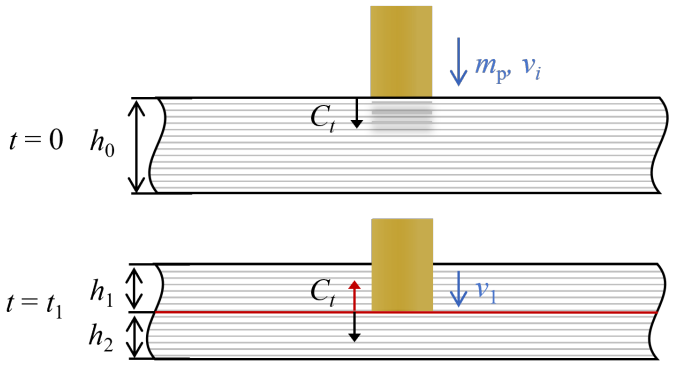

Figure 3: Schematic of the local penetration phase. The perforation depth is dictated by the propagation and reflection of compression waves.

Phase I ends at the time instant $t = t_1$ when the compression wave reaches the bottom of the UHMWPE composite and reflects with a travelling distance of $2h_0 - h_1$. The duration for phase I was therefore:

$$t_1 = (2h_0 - h_1)/C_t. \tag{4}$$

The penetration depth h_1 can be obtained by integrating Eq. 3 with time:

$$h_1 = \int_0^{t_1} v_i e^{-\rho C_t A_p t/m_p} dt. \tag{5}$$

Duration t_1 and penetration depth h_1 can be solved from Eqs. 4 and 5 for a given initial velocity v_i. The projectile velocity at the end of phase I is written as:

$$v_1 = v(t = t_1) = v_i e^{-\rho C_t A_p t_1/m_p} \tag{6}$$

which serves as the initial condition for phase II.

2.3. Phase II response (transverse bulging deformation with progressive penetration): $t_1 < t \le t_f$

2.3.1. Equation of motion

In Phase II, the laminated plate with an intact thickness of $h_2 = h_0 - h_1$ was subjected to impact by the projectile with a velocity of v_1, which developed transverse bulging deformation (TBD). As the

flexural wave propagates outward from the impact point, the laminated plate undergoes transient deformation within a certain region according to the travelling hinge location, as illustrated in Fig. 4. The travelling hinge position, denoted as $\zeta(t)$, advances toward the fixed boundaries ($x = a$ and $y = a$) over time. Once the travelling hinges coalesce with the boundary, it becomes a stationary one, i.e., $\zeta(t) = a$. For square laminated plates, the travelling hinges' motion in both the $x-$ and $y-$ directions are identical [31, 35]. It is assumed that the transverse normal remains perpendicular to the mid-surface after deformation.

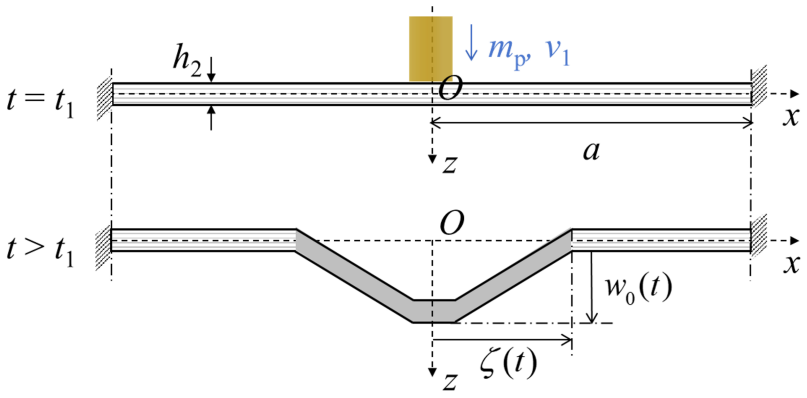

Figure 4: Schematic of the transverse bulging deformation mechanism in phase II.

In the modal analysis, it assumes that the ballistic response of the laminated plate results in deformation that continually evolves towards a modal solution, i.e. the velocity field $\dot{w}$ can be written as the product of separate functions of space and time $\dot{w}(x, y, t)$. The modal solution is a velocity field with separated functions for spatial and temporal variables. The admissible transverse velocity field and shear deformation profiles used in [32] (originally for impact response of laminated glass) were adopted here:

$$\dot{w}(x, y, t) = \dot{w}_0(t)\Big[1 - \frac{2x^2}{\zeta(t)^2} + \frac{x^3}{\zeta(t)^3}\Big]\Big[1 - \frac{2y^2}{\zeta(t)^2} + \frac{y^3}{\zeta(t)^3}\Big] \tag{7}$$

and

$$\gamma^0_{xz}(x, y, t) = \gamma_{xz0}(t) \sin\Big[\frac{\pi x}{2\zeta(t)}\Big] \cos\Big[\frac{\pi y}{2\zeta(t)}\Big] \tag{8a}$$

$$\gamma^0_{yz}(x, y, t) = \gamma_{yz0}(t) \cos\Big[\frac{\pi x}{2\zeta(t)}\Big] \sin\Big[\frac{\pi y}{2\zeta(t)}\Big] \tag{8b}$$

where $\dot{w}_0(t)$ is the velocity at the plate's centre; the product of second and third terms in Eq. 7 is the *mode function* or *mode shape* that is governed by the travelling hinge position $\zeta(t)$ in $x-$ and $y-$ directions; $\gamma_{xz0}(t)$ and $\gamma_{yz0}(t)$ are shear displacements. In regions where $x > |\zeta(t)|$ and $y > |\zeta(t)|$, the laminated plate is assumed to remain undeformed, i.e., $\dot{w}_0(t) = 0$. After the hinge reaches the boundary, $\zeta(t) = a$ is substituted into Eqs. 7. Notice that the corresponding modal displacement (w_0) and acceleration ($\ddot{w}_0$) fields can also be written in the same partial functions.

The total kinetic energy of a quarter of the model (target and projectile) at any given moment t can be expressed as:

$$T = \frac{1}{2}\mu \int_0^{\zeta(t)} \int_0^{\zeta(t)} \dot{w}^2(x, y, t)\mathrm{d}x\mathrm{d}y + \frac{1}{8} m_p \dot{w}_0^2(t) \tag{9}$$

where $\mu = \rho h$ is the areal density of the intact laminated plate.

We now proceed to derive expressions for the total strain energy of the panel by first establishing the constitutive equation that relates the bending moment M, membrane force N and transverse shear force Q to the strains. Here, the first-order shear deformation plate theory is employed, which incorporates the effect of bending, membrane and transverse shear and uses damage mechanics to capture the progressive through-thickness fracture.

The components of stress σ in the laminated plate give rise to the following force resultants for bending moment M, membrane force N and shear force Q given by

$$\begin{Bmatrix} N_{xx} \\ N_{yy} \\ N_{xy} \end{Bmatrix} = \int_{-h/2}^{h/2} \begin{Bmatrix} \sigma_{xx} \\ \sigma_{yy} \\ \sigma_{xy} \end{Bmatrix} \mathrm{d}z \quad \begin{Bmatrix} M_{xx} \\ M_{yy} \\ M_{xy} \end{Bmatrix} = \int_{-h/2}^{h/2} \begin{Bmatrix} \sigma_{xx} \\ \sigma_{yy} \\ \sigma_{xy} \end{Bmatrix} z\mathrm{d}z \quad \begin{Bmatrix} Q_x \\ Q_y \end{Bmatrix} = \int_{-h/2}^{h/2} \begin{Bmatrix} \sigma_{xz} \\ \sigma_{yz} \end{Bmatrix} \mathrm{d}z. \tag{10}$$

where h is the thickness of the intact laminated plate.

The linear-elastic constitutive relation between the stress and strain components for the laminated plate is

$$\begin{Bmatrix} \sigma_{xx} \\ \sigma_{yy} \\ \sigma_{yz} \\ \sigma_{xz} \\ \sigma_{xy} \end{Bmatrix} = \begin{Bmatrix} Q_{11} & Q_{12} & 0 & 0 & 0 \\ Q_{12} & Q_{22} & 0 & 0 & 0 \\ 0 & 0 & Q_{44} & 0 & 0 \\ 0 & 0 & 0 & Q_{44} & 0 \\ 0 & 0 & 0 & 0 & Q_{66} \end{Bmatrix} \begin{Bmatrix} \epsilon_{xx} \\ \epsilon_{yy} \\ \gamma_{yz} \\ \gamma_{xz} \\ \gamma_{xy} \end{Bmatrix} \tag{11}$$

where Q_{ij} are the plane stress-reduced stiffness components; $Q_{11} = E_1/(1 - \nu_{12}\nu_{21})$, $Q_{22} = E_2/(1 - \nu_{12}\nu_{21})$, $Q_{12} = Q_{21} = \nu_{12}Q_{11}$, $Q_{44} = Q_{22} = Q_{11}$ and $Q_{66} = G_{12}$. Here, E_1 and E_2 are Young's moduli in the 0° and 90° material directions, respectively, ν_{12} and ν_{21} are the Poisson's ratios, and G_{12} is the in-plane shear modulus. Notice that isotropic material properties were assumed for the laminated plate, i.e. $E_1 = E_2$.

The strain components have the form,

$$\begin{Bmatrix} \epsilon_{xx} \\ \epsilon_{yy} \\ \gamma_{yz} \\ \gamma_{xz} \\ \gamma_{xy} \end{Bmatrix} = \begin{Bmatrix} \epsilon_{xx}^0 \\ \epsilon_{yy}^0 \\ \gamma_{yz}^0 \\ \gamma_{xz}^0 \\ \gamma_{xy}^0 \end{Bmatrix} + z \begin{Bmatrix} \epsilon_{xx}^1 \\ \epsilon_{yy}^1 \\ 0 \\ 0 \\ \gamma_{xy}^1 \end{Bmatrix} \tag{12}$$

where $(\epsilon_{xx}^0, \epsilon_{yy}^0, \gamma_{xy}^0)$ are the membrane strains expressed as a function of admissible displacement field (see Eq. 7),

$$\epsilon_{xx}^0 = \frac{1}{2}\Big[\frac{\partial W(x, y, t)}{\partial x}\Big]^2 \quad \epsilon_{yy}^0 = \frac{1}{2}\Big[\frac{\partial W(x, y, t)}{\partial y}\Big]^2 \quad \gamma_{xy}^0 = \frac{\partial W(x, y, t)}{\partial x}\frac{\partial W(x, y, t)}{\partial y} \tag{13}$$

and $(\epsilon^1_{xx}, \epsilon^1_{yy}, \gamma^1_{xy})$ are the bending strains, also known as curvatures, written as

$$\epsilon^1_{xx} = \frac{\partial\theta_x(x,y,t)}{\partial x} \quad \epsilon^1_{yy} = \frac{\partial\theta_y(x,y,t)}{\partial y} \quad \gamma^1_{xy} = \frac{\partial\theta_x(x,y,t)}{\partial y}\frac{\partial\theta_y(x,y,t)}{\partial x} \tag{14}$$

in which the rotations of a transverse normal about y and x axis are respectively

$$\theta_x(x,y,t) = \gamma_{xz}(x,y,t) - \frac{\partial W(x,y,t)}{\partial x} \tag{15a}$$

$$\theta_y(x,y,t) = \gamma_{yz}(x,y,t) - \frac{\partial W(x,y,t)}{\partial y}. \tag{15b}$$

Substituting Eqs. 11 and 12 into Eq. 10 and re-arranging give the constitutive equations:

$$\begin{Bmatrix} N_{xx} \\ N_{yy} \\ N_{xy} \end{Bmatrix} = \begin{Bmatrix} A_{11} & A_{12} & 0 \\ A_{12} & A_{11} & 0 \\ 0 & 0 & A_{66} \end{Bmatrix} \begin{Bmatrix} \epsilon^0_{xx} \\ \epsilon^0_{yy} \\ \gamma^0_{xy} \end{Bmatrix} \tag{16a}$$

$$\begin{Bmatrix} M_{xx} \\ M_{yy} \\ M_{xy} \end{Bmatrix} = \begin{Bmatrix} D_{11} & D_{12} & 0 \\ D_{12} & D_{11} & 0 \\ 0 & 0 & D_{66} \end{Bmatrix} \begin{Bmatrix} \epsilon^1_{xx} \\ \epsilon^1_{yy} \\ \gamma^1_{xy} \end{Bmatrix} \tag{16b}$$

$$\begin{Bmatrix} Q_x \\ Q_y \end{Bmatrix} = K\frac{1-\nu}{2} \begin{Bmatrix} A_{11} & 0 \\ 0 & A_{11} \end{Bmatrix} \begin{Bmatrix} \gamma^0_{xz} \\ \gamma^0_{yz} \end{Bmatrix} \tag{16c}$$

where K is the shear correction factor; note that in Mindlin's plate theory, $K = 5/6$ for rectangular cross-sections; A_{ij} and D_{ij} are extensional and bending stiffnesses, which are defined in terms of the lamina stiffness Q_{ij} as

$$(A_{ij}, D_{ij}) = \int_{-h/2}^{h/2} Q_{ij}(1, z^2)\mathrm{d}z. \tag{17}$$

The strain energy for the quarter of a laminated plate can be written as:

$$\begin{aligned}\Pi = \Pi_b + \Pi_m + \Pi_s = \frac{1}{2}\int_0^b\int_0^a [M_{xx}\epsilon^1_{xx} + M_{yy}\epsilon^1_{yy} + M_{xy}\gamma^1_{xy}]\mathrm{d}x\mathrm{d}y \\ + \frac{1}{2}\int_0^b\int_0^a \lambda[N_{xx}\epsilon^0_{xx} + N_{yy}\epsilon^0_{yy} + N_{xy}\gamma^0_{xy}]\mathrm{d}x\mathrm{d}y + \frac{1}{2}\int_0^b\int_0^a [Q_x\gamma^0_{xz} + Q_y\gamma^0_{yz}]\mathrm{d}x\mathrm{d}y.\end{aligned} \tag{18}$$

where $0 \leq \lambda \leq 1$ is a membrane 'knock-down' factor so that $\lambda = 0$ corresponds to the condition when the boundary provides zero resistance to plate pull-in, whereas $\lambda = 1$ corresponds to the condition when there is strictly no pull-in so that the full membrane effect develops. Due to the insufficient clamping force at the boundary, in-plane deformation (also known as the 'pulling-in effect') emanated from the boundary edges as observed from the experiment [17]. In the large deflections of plate theory by Timoshenko and Woinowsky-Krieger[38], it was also suggested that when the edge is free to move in the radical direction, the membrane stretching effect should be

much less than that of a fully clamped boundary. It is often difficult to model the real boundary conditions of any experiment. Hence, the factor λ is employed here to modulate the influence of membrane stretch, and its concomitant effect on the reduction of the membrane energy component in Eq. 18 was accounted for by adjusting the membrane 'knock-down' factor λ, with $\lambda = 1$ and $\lambda = 0$ corresponding the lower and upper bounds of the current prediction. The value of λ will be calibrated based on the experimental results in the literature.

Given that *Lagrangian* of a quarter of the laminated plate is:

$$\mathcal{L} = T + \Pi, \tag{19}$$

the equation of motion governing $w_0(t)$, $\zeta(t)$, $\gamma_{xz0}(t)$ and $\gamma_{yz0}(t)$ are found by solving the well-known Lagrange equation of the 2nd kind numerically:

$$\frac{\mathrm{d}}{\mathrm{d}t}\Big(\frac{\partial \mathcal{L}}{\partial \dot{w}_0}\Big)+\frac{\partial \mathcal{L}}{\partial w_0} = 0, \quad \frac{\mathrm{d}}{\mathrm{d}t}\Big(\frac{\partial \mathcal{L}}{\partial \dot{\zeta}}\Big)+\frac{\partial \mathcal{L}}{\partial \zeta} = 0, \quad \frac{\mathrm{d}}{\mathrm{d}t}\Big(\frac{\partial \mathcal{L}}{\partial \dot{\gamma}_{xz0}}\Big)+\frac{\partial \mathcal{L}}{\partial \gamma_{xz0}} = 0, \quad \frac{\mathrm{d}}{\mathrm{d}t}\Big(\frac{\partial \mathcal{L}}{\partial \dot{\gamma}_{yz0}}\Big)+\frac{\partial \mathcal{L}}{\partial \gamma_{yz0}} = 0. \tag{20}$$

The above ordinary differential equations (ODEs) are solved numerically using the fourth-order Runge-Kutta method with the following initial conditions:

$$w_0(t = t_1) = 0 \quad \dot{w}_0(t = t_1) = v_1 \quad \zeta(t = t_1) = 0 \tag{21}$$

where v_1 was the projectile velocity at the end of phase I in Eq. 6.

When the ODEs were solved, the remaining thickness of the intact plate h must be updated during each iteration. The remaining thickness depends upon the extent of penetration into the composite plies. To calculate the thickness of the intact composite (or the penetration depth), the thickness at the beginning of phase II was pre-discretised into h_2/h_L number of layers with h_L being the sub-laminate thickness. During each time iteration, the damage of the impact-receiving layer that is in contact with the projectile is evaluated by the damage criteria in Section 2.3.2. If damage occurs, thickness is updated in the next time step, i.e. $h = h - h_L$.

Phase II ends either when the projectile and laminated plate cease motion, i.e. $\dot{w}_0(t = t_f) = 0$ when $h(t = t_f) > 0$, or when full penetration occurs $h < 0$ leading to a finite value of residual velocity $\dot{w}_0(t = t_f) > 0$. The initial velocity v_i that corresponds to the critical condition of $\dot{w}_0(t = t_f) = 0$ and $h(t = t_f) = 0$ refers to the ballistic limit velocity v_{bl} which can be obtained by incrementally increasing the value of v_i.

2.3.2. Damage criteria

The progressive failure mechanism in phase II is depicted in Fig. 5. The composite plies can fail either by a mixed mode failure or tensile failure [36] in phase II. When the deformation is developed during phase II, the composite plies fail under combined stress rather than pure transverse shear. On the other hand, tensile fracture could occur at individual composite ply due to transverse bulging deflection.

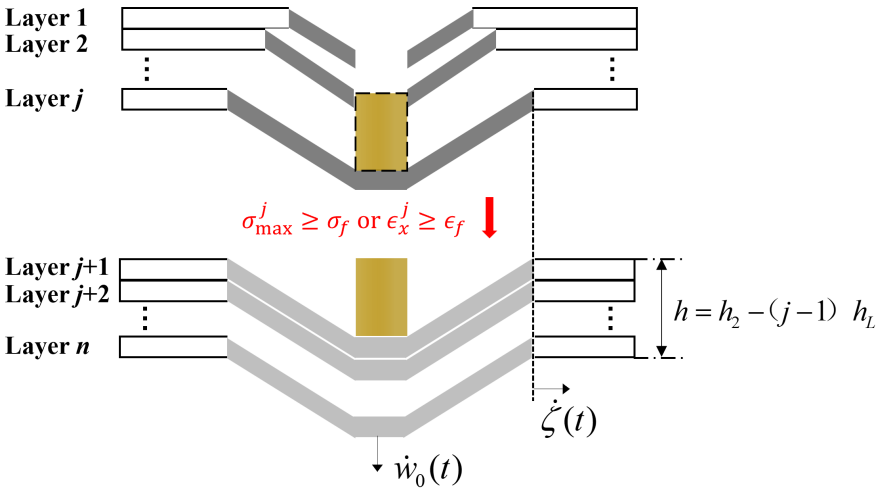

Figure 5: Schematic of deformation and failure of discretised layers in phase II. After the projectile penetrates the jth layer, the substrate layers resist the foreign load together until failure occurs in the $j+1$th layer.

The maximum equivalent stress criterion is used herein to predict the *mixed mode failure* of the individual layer:

$$D_1 = \frac{\sigma^j_{\max}}{\sigma_f} \tag{22}$$

where D_1 is the damage parameter; $\sigma^j_{\max}$ denotes the maximum equivalent stress of the jth layer; σ_f is the failure stress.

The equivalent stress is found to be greatest at the centre of the laminated plate (this will be confirmed later in Section 4.1) such that

$$\sigma^j_{\max} = \sigma^j_{\text{eq}}(x=0, y=0) = \sqrt{(\sigma^j_{xx} + \sigma^j_{yy})^2 - 3(\sigma^j_{xx}\sigma^j_{yy} - \sigma^j_{xy}\sigma^j_{xy})}. \tag{23}$$

Tensile failure occurs when the tensile strain reaches the failure strain:

$$D_2 = \frac{\epsilon^j_x}{\epsilon_f} \tag{24}$$

where D_2 is the damage parameter; ϵ_f is the failure strain in the maximum sense, i.e., the maximum between fracture strains in a uniaxial tensile test and in a shear test $\epsilon_f = max(\epsilon_{xx}, \gamma_{xy})$ [39]. In Eq. 24, the tensile strain is expressed as a function of transverse central deflection $w_0(t)$ [40]:

$$\epsilon^j_x = \frac{w_0(t)}{4\zeta(t)} \frac{w_0(t)}{2h}. \tag{25}$$

When either D_1 or D_2 reaches unity, failure occurs at the jth layer, which updates the value of remaining thickness in the next time step for the equation of motion, i.e. $h = h_2 - (j-1)h_L$. the

projectile was assumed to impact the subsequent layer $(j+1)$ without deceleration, the interaction of which could lead to further penetration according to Eq. 22 or Eq. 24.

3. Validation

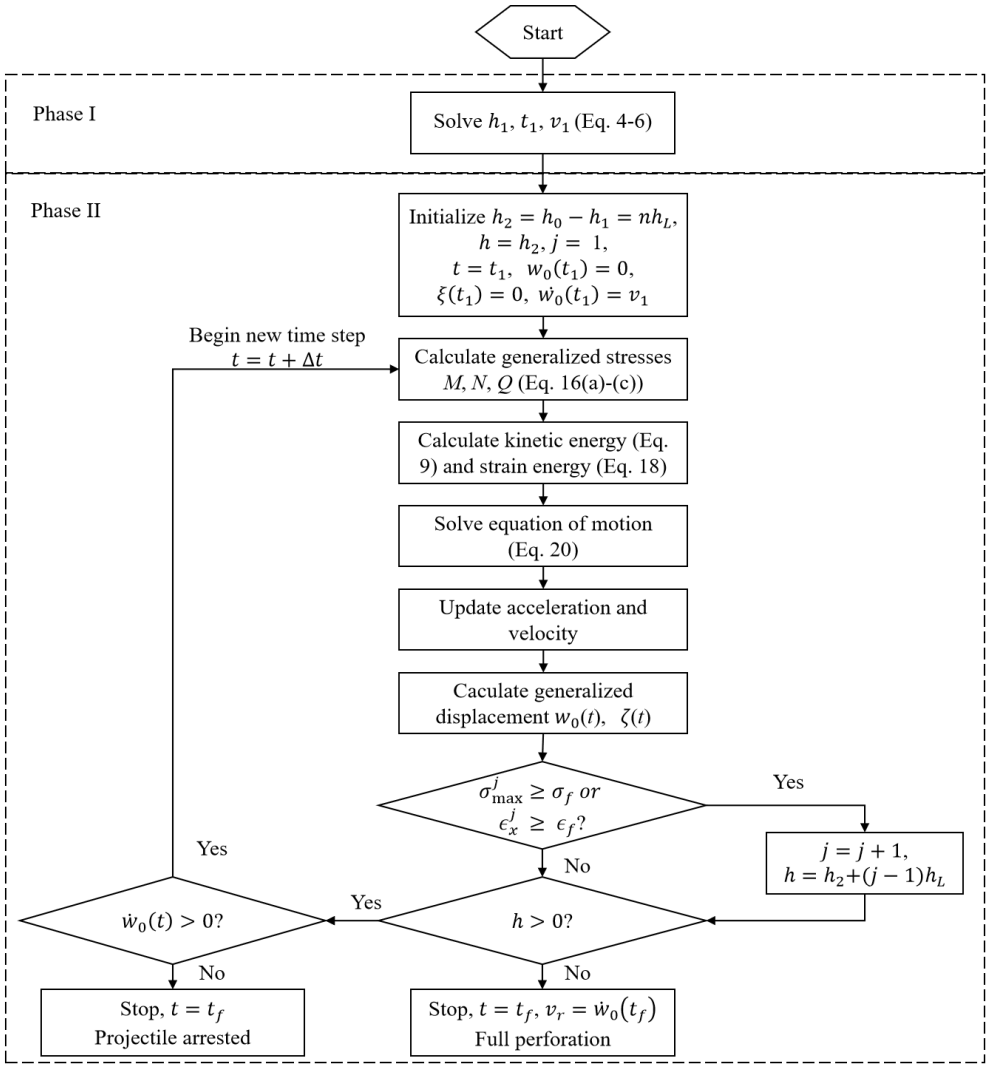

Figure 6: Flow-chart on the numerical implementation of the analytical model in Section 2.

Analytical predictions of the TBD and ballistic limit velocity will now be validated against the experimental data of HB26 UHMWPE laminates by Nguyen et al. [17]. The numerical predictions in [17] are also included for comparison. The square UMHWPE laminated plate has an edge length of $2a = 0.3$ m. Each homogenised layer's thickness is $h_L = 0.24$ mm since the thickness of a single ply is 60 μm according to [34]. Two projectile diameters, 12.7 mm and 20 mm, were used in [17]. The thickness of the specimen ranged from 9 mm to 75 mm. The material properties of the HB26 laminated plate (in the corresponding experiments) are tabulated in Table 2. A flow chart on the numerical implementation of Section 2 is shown in Fig. 6.

Table 2: The material properties of HB26 UHMWPE laminates used in the current analytical model.

Material property	Value	Reference
ρ_0 (kg/m^3)	980	[17]
E_1, E_2 (GPa)	51.1	[17]
E_3 (GPa)	3.62	[17]
G_{12} (GPa)	0.19	[17]
σ_f (GPa)	10	[17]
ϵ_f	0.8	[39]

3.1. TBD and travelling hinge position

Figure 7 compares the analytical predictions of transient TBD and travelling hinge position to the experimental results in the work by Nguyen et al. [17] for HB26 UMHWPE laminated plate targets with three different thicknesses. Notice that the ballistic loads in all three tests were not sufficiently intense to cause full penetration. The predicted temporal evolution of TBD with $\lambda = 0$ agrees well with the experimental counterpart, including the maximum transverse bulging deflection and the time instant at which the maximum w_0 was reached, as can be seen in Figs. 7a, 7c and 7e. Unsurprisingly, prediction of TBD with $\lambda = 1$ was significantly less than that with $\lambda = 0$ due to more structural resistance from the membrane action. Since the prediction based on the value of $\lambda = 0$ leads to the best fit with the experimental data, this value will be used throughout this work. Using $\lambda = 0$ would neglect the contribution from membrane effect. This coincides with the analytical work by Liu et al. [41] who neglected the membrane effect and used a SDOF model with only a bending stiffness to predict the large deflection response of UHWMPE composite under impact loading, the results of which agreed well the their experimental data. Unlike monolithic (metallic) plates, it is *conjectured* that the interlaminar strength of a composite plate does not typically offer sufficient resistance against pull-in and it is also impossible to replicate a through-thickness 'fully-clamped' boundary condition experimentally for any composite plate. Unlike [41], this work has laid a theoretical foundation which considers the effect of bending moment, membrane force and transverse shear during the dynamic response of UHMWPE composite under ballistic loading. Readers can adjust the effects of membrane force by changing the value of λ depending on the support condition. It is worth highlighting that in the case of body armour - this is mostly likely to be unsupported along the boundary - substantial pulling-in effect is expected. In this case, the membrane effect can be compensated by choosing a small value of λ.

The analytical model successfully predicts the monotonic increase of dimensionless hinge position ζ/a over time, corroborating the expansion of the deformation region during the impact event. However, the analytical model with $\lambda = 0$ over-predicts the dimensionless hinge position after $t' = 200$ μs. The overprediction is more evident in relatively thick targets, i.e. $h_0 = 20$ and 36 mm. The discrepancy may be due to the 'pulling-in' effect resulting from a lack of clamping force in the experiments where significant in-plane displacement of the composite at the boundary was observed in the experiments. Therefore, it was difficult for the hinge to reach the boundary in the

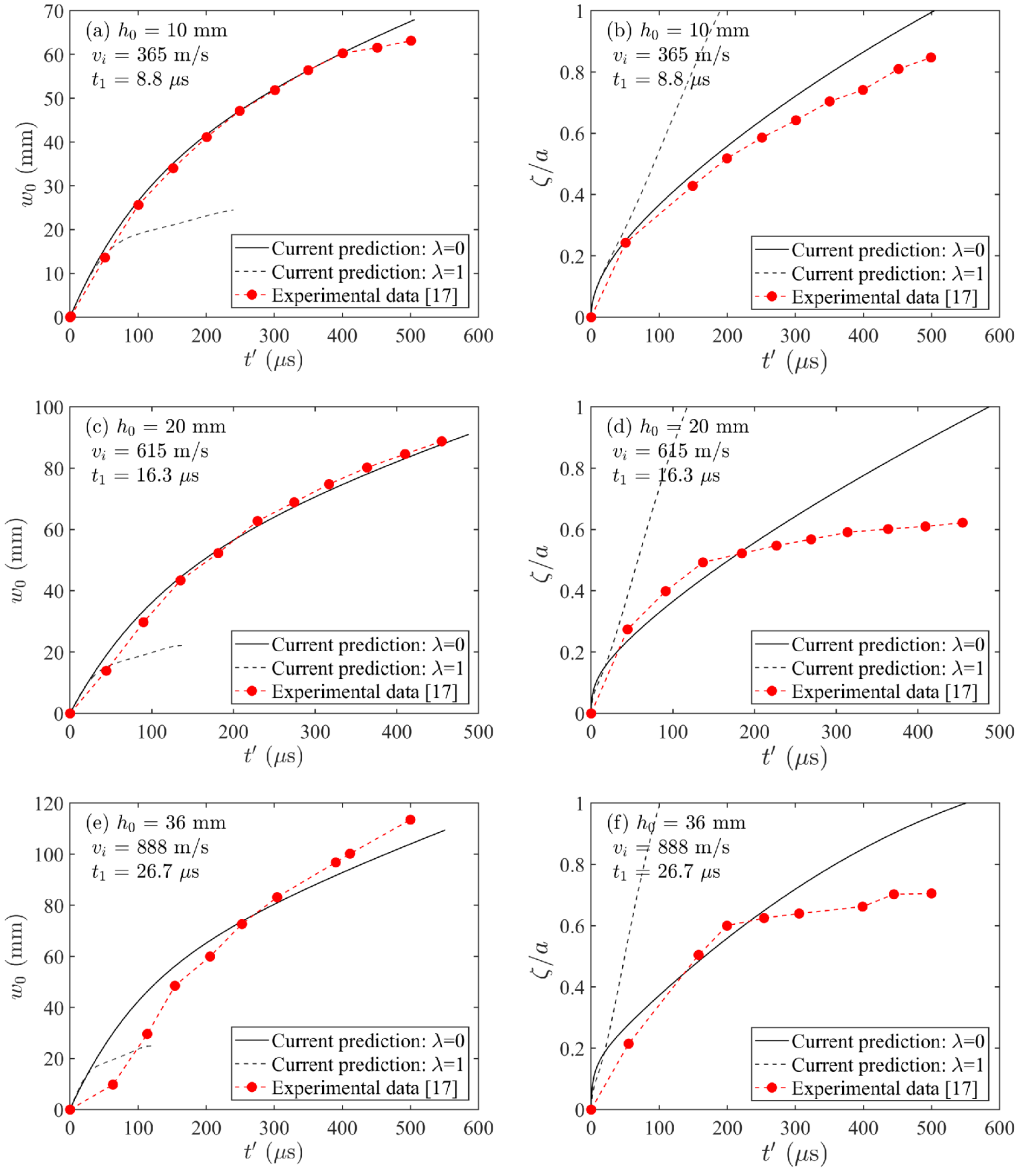

Figure 7: Comparison between the analytical predictions and the experimental data in [17] for HB26 UHMWPE laminates of three different thicknesses ($h_0 = 10, 20, 36$ mm): transient bulging deflection $w_0(t)$ (left column) and dimensionless hinge position $\zeta(t)/a$ (right column). The blunt projectile has a diameter of $2R$=20 mm. Notice that in the experimental work of [17], the time duration for phase I was not reported. In this case, w_0 was plotted as a function of $t' = t - t_1$ to allow the comparison to be made. The value of t_1 in the analytical prediction was inserted in each subfigure. $\lambda = 1$ and $\lambda = 0$ refer to the lower and upper bounds of the current prediction respectively.

298 experiments.

3.2. *Ballistic limit*

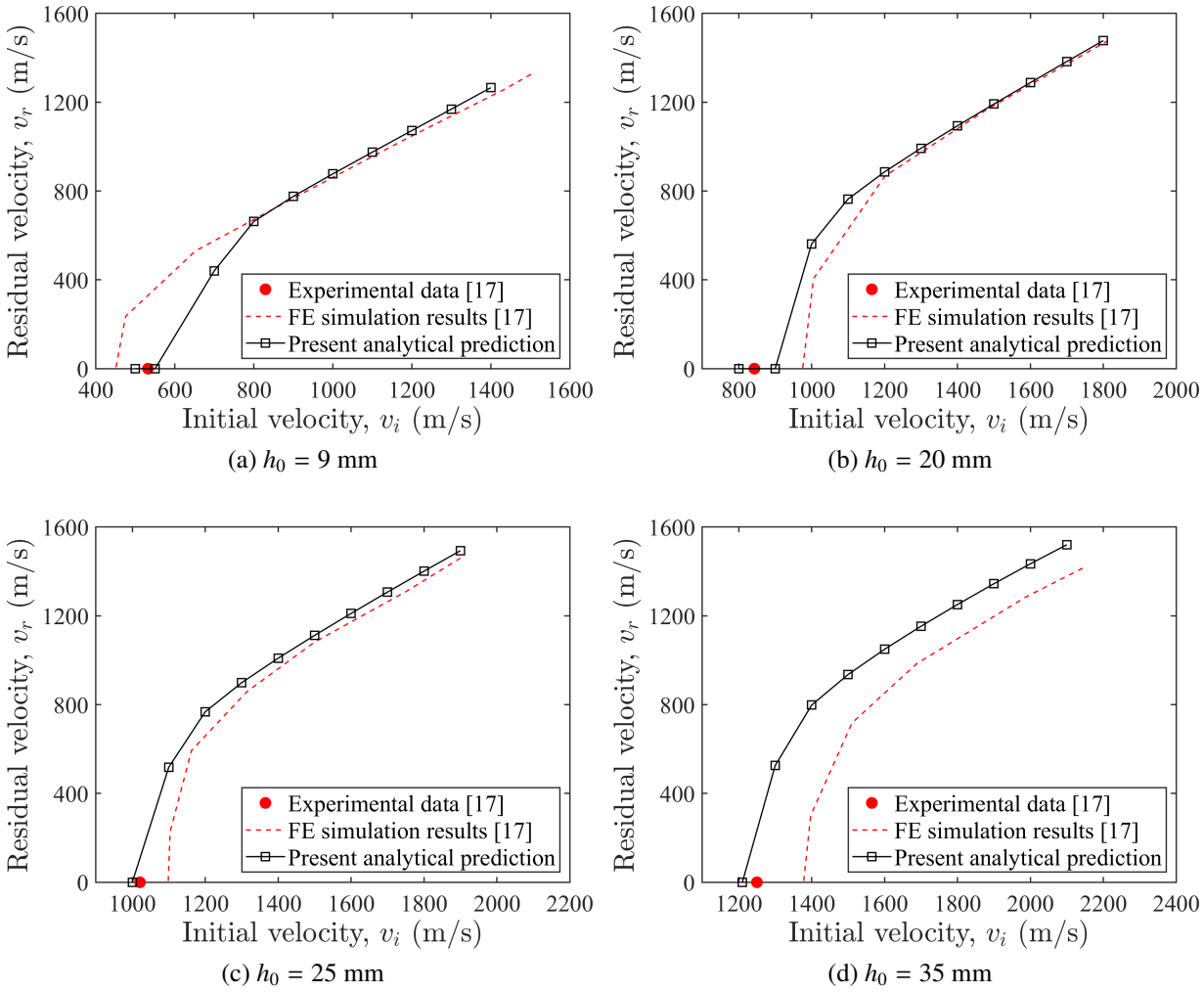

Figure 8: Comparison between analytical predicted residual velocity and published data [17] for HB26 UHMWPE laminates of four different thicknesses ($h_0 = 9, 20, 25, 35$ mm). The blunt projectile has a diameter of $2R = 12.7$ mm.

The predicted residual velocities with $\lambda = 0$ are compared to the corresponding data (numerical and experimental) in the literature for ballistic impact in Figs 8 and 9. In general, the analytical model is capable of predicting the ballistic curve of UHMWPE composite for a wide range of thicknesses ($10 \leq h_0 \leq 75$ mm) under two different projectile diameters ($2R = 12.7$ and 20 mm). For the ballistic impact under two projectile sizes, the current prediction of residual velocity agrees well with the finite element results in [17] for all the target thicknesses with the notable exceptions of $h_0 = 35$ mm, $2R$ =12.7 mm and $h_0 = 75$ mm, $2R$ =20 mm where the current prediction of residual velocity is greater than that predicted by the numerical model in [17]. The intersection of the ballistic curve to the x-axis in Figs. 8 and 9 refers to the ballistic limit velocity. In the current analytical model, ballistic limit velocity can be obtained by finding the initial velocity of

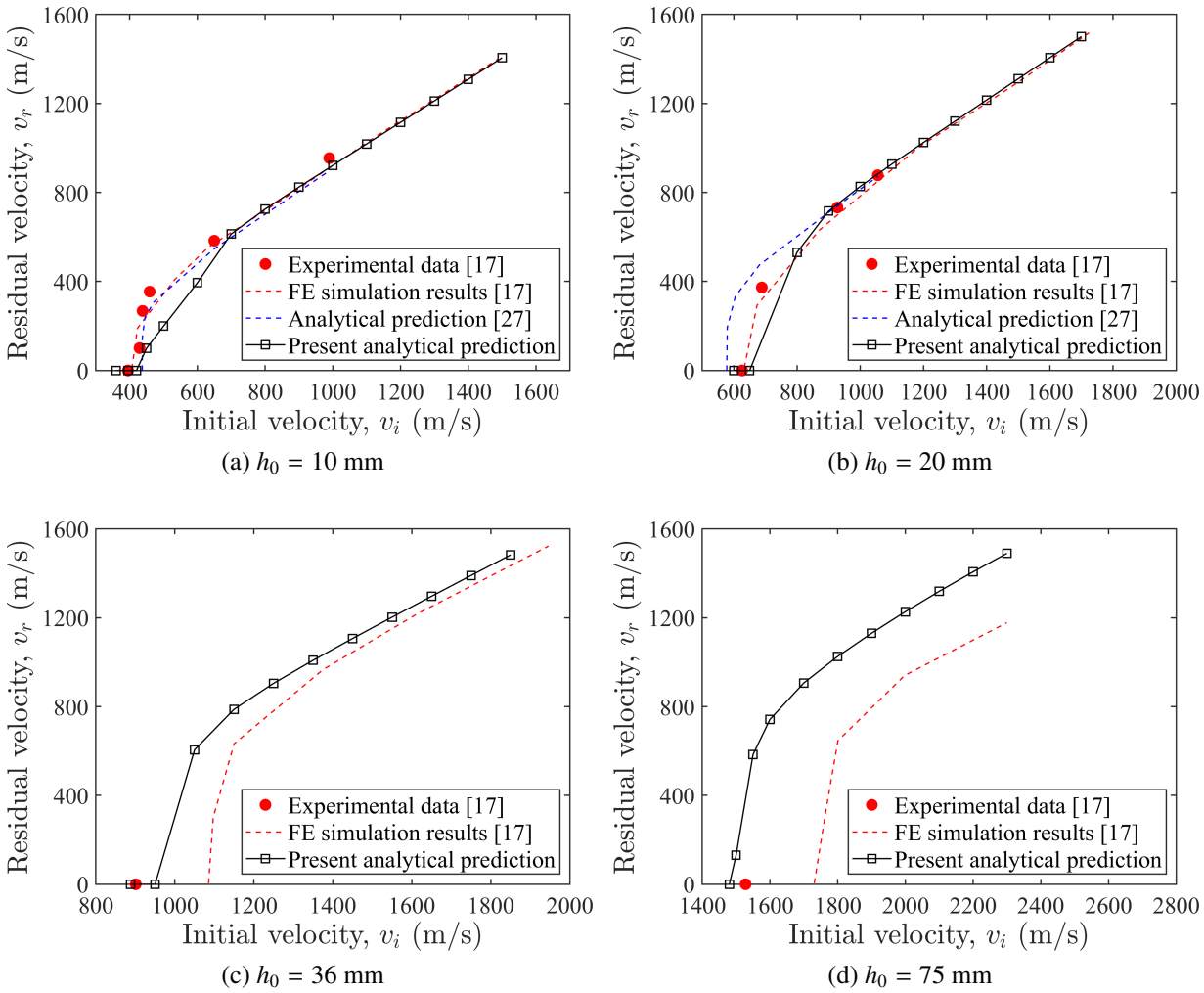

(a) h_0 = 10 mm (b) h_0 = 20 mm

(c) h_0 = 36 mm (d) h_0 = 75 mm

Figure 9: Comparison between analytical predicted residual velocity and published data [17] for HB26 UHMWPE laminates of four different thicknesses ($h_0 = 10, 20, 36, 75$ mm). The blunt projectile has a diameter of $2R$ =20 mm. The analytical prediction by Zhang et al. [27] was also inserted for comparison for cases of h_0 = 10 and 20 mm.

the projectile to cause complete penetration of the target with zero residual velocity in an iterative process. The analytical predictions of ballistic limit velocities were in excellent correlation with the experimental counterpart as seen in Figs. 10a and 10b.

4. Discussion

In this section, the validated model is employed to provide further insights into the dynamic failure behaviour, travelling hinge phenomenon and the effect of impact velocity during the ballistic impacts of UMHWPE laminated plate. A typical laminated plate with material properties and in-plane dimensions identical to those studied in the preceding section was used here. A thickness of

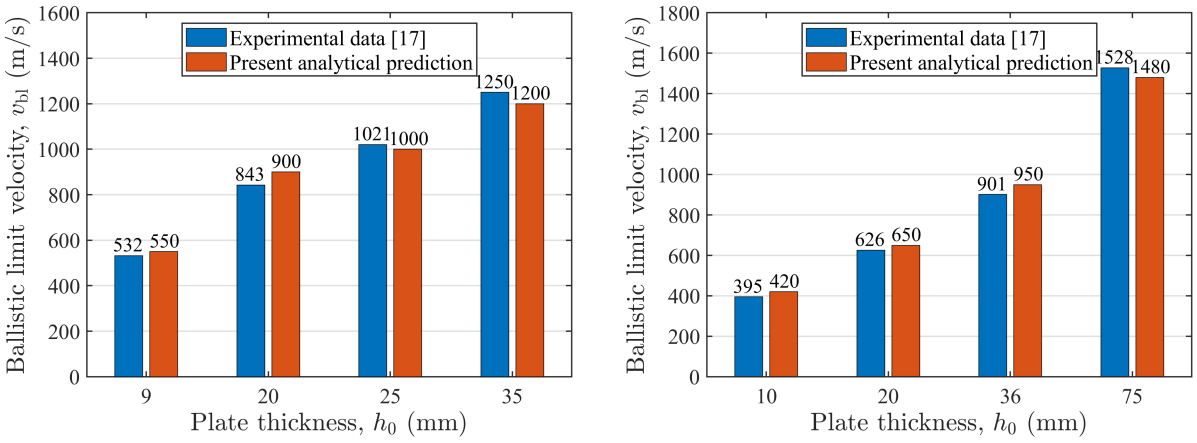

(a) (b)

Figure 10: Comparison between analytical prediction and published data [17] for ballistic limit velocity under blunt projectiles of diameters of (a) $2R$=12.7 mm and (b) $2R$=20 mm.

36 mm and a projectile diameter of 20 mm were used throughout this section.

4.1. Evolution of damage

To provide insights into the evolution of failure, damage parameters D_1 and D_2 were plotted as a function of time in Fig. 11a at v_i = 888 m/s. The initial velocity was deliberately chosen to be below the ballistic limit velocity (901 m/s). The horizontal dash line refers to the critical condition of the damage parameters reaching unity. Failure, due to either mixed mode failure or tensile failure, would not take place if the damage curve is below this horizontal dash line. Part of the figure ($27 \leq t \leq 50\mu$s) was magnified to showcase the prediction of equivalent stress at the laminated plate centre during the initial response in phase II. It can be seen that the maximum equivalent stress criterion (Eq. 22) was satisfied at the outset of the phase II response, leading to the instant failure of the impact-receiving layer. The damage parameter D_1 then oscillates close to the value of one. The intersection points of the black curve with the horizontal dash line ($D_1 = 1$) refer to the time instants when progressive layer-by-layer damage happens across the thickness. After $t > 50$ μs, the damage parameter D_1 reduces monotonically with time indicating that mixed mode failure was absent. This prediction coincides to that in the analytical work by Olsson [37] who also showed that the stress predicted by classical plate theory increases and then decreases over time for composite plates. The red solid curve in Fig. 11a denotes the time history of the damage parameter for the tensile failure D_2, which increases monotonically with time. The maximum value of D_2 at t_f = 536 μs was less than unity, corroborating that tensile failure was absent. That damage parameter D_1 or D_2 is less than unity when the projectile's velocity reduces to zero confirms that full penetration did not take place, which is in line with the experimental observation.

Figure 11b shows the corresponding analytical prediction of the temporal evolution of the thickness for the intact composite in phase I and II response. The thickness drops from 36 mm to 15.2

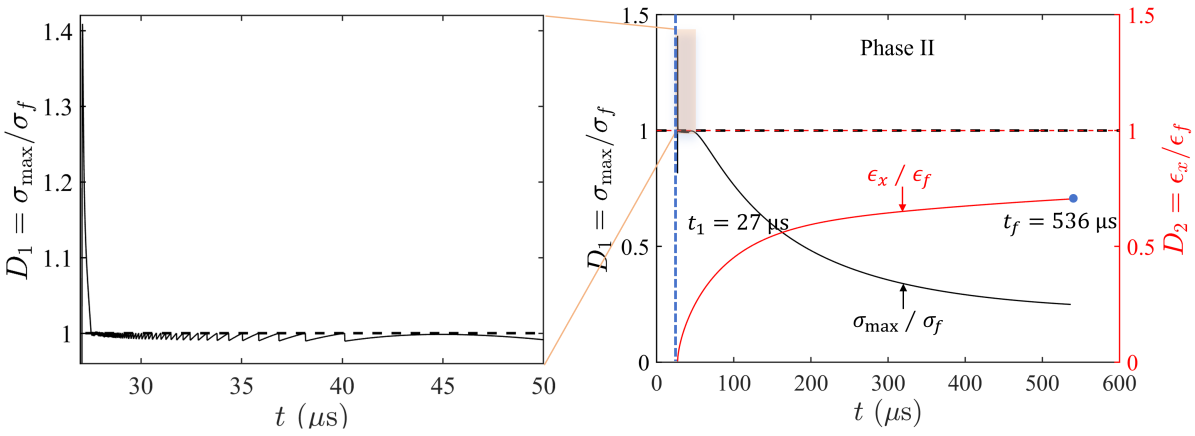

(a) Evolution of damage parameter

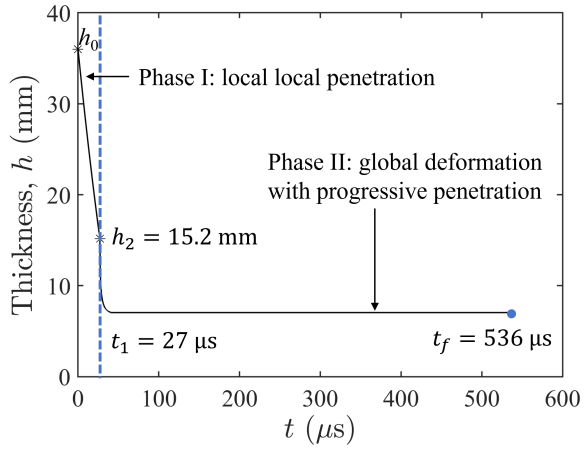

(b) Thickness of intact composite during phase I and II

Figure 11: Analytical predictions of the time-history of (a) damage parameters, (b) thickness of intact composite for 36 mm thick laminated plate impacted by a projectile of diameter $2R$ =20 mm at v_i =888 m/s. The projectile did not penetrate completely the target.

mm during the local penetration (phase I) under only 27 μs. In phase II, mixed-mode failure occurs continuously at the impact-receiving layer, albeit only for a short period of 13 μs. The UMHWPE laminated plate has a remaining thickness of 7.5 mm to withstand the projectile until it is fully arrested.

The analytical prediction of the evolution of equivalent stress distribution (Eq. 23) for the same impact case in Fig. 11 was shown in Fig. 12. The stress contour on the impact-receiving layer (the sub-laminate that was in contact with the projectile) was given. The prediction was mapped across the symmetrical planes to showcase the stress contour on the entire plane. The maximum equivalent stress was found to be always at the centre at different time frames, which justifies the assumption made in the analytical model regarding Eq. 23. The equivalent stress was localised at the central region in the vicinity of the impact at the initial stage in phase II. A more uniform dis-

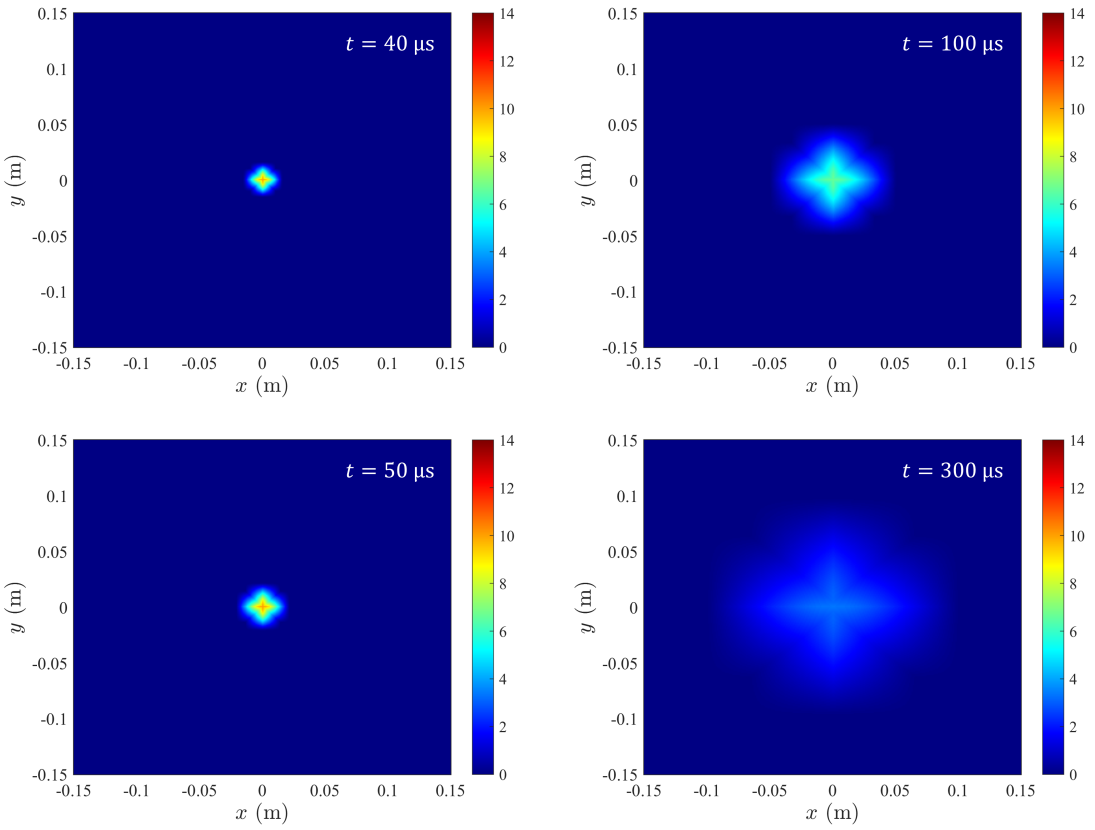

Figure 12: Analytical prediction of the evolution of equivalent stress contours (in GPa) on the impact-receiving layer of a 36 mm thick laminated plate impacted by a blunt projectile of diameter $2R$ =12.7 mm at v_i =888 m/s. The projectile was arrested at the time instant of t_f = 536μs.

tribution of the equivalent stress was noted with the passage of time. The spread of the equivalent stress is attributed to the high wave speed of the UMHWPE laminated plate which is beneficial to transform a local impact to a global response. The hinge reaches the boundary at the cessation of motion according to Fig. 7f.

Figure 13 and 14 present the analytical predictions for the ballistic impact case of v_i =1200 m/s. The initial velocity was deliberately chosen to exceed the ballistic limit velocity. The time history of damage parameters, the remaining thickness of intact composite, projectile velocity and hinge position were plotted in Figs. 13a, 13b, 13c and 13d respectively. In phase I, projectile velocity reduces from 1200 to 922 m/s (in Fig. 13c) with a significant penetration depth of 25.8 mm (in Fig. 13b). Phase II begins with the initial condition of v_1 = 922 m/s and h_2 = 10.2 mm. As seen in Fig. 13a, the stress-based damage parameter D_1 drops quickly to unity, and maintains at one until t_f =67 μs, which indicates that progressive ply-by-ply failure occurs continuously in phase II. The stress-based damage is more dominant than the strain-based damage since D_1 is greater than D_2 for the majority of the response. D_2 finally increases up to unity at t = 67 μs, at which instant the remaining composite abruptly ruptures almost instantaneously, as seen in

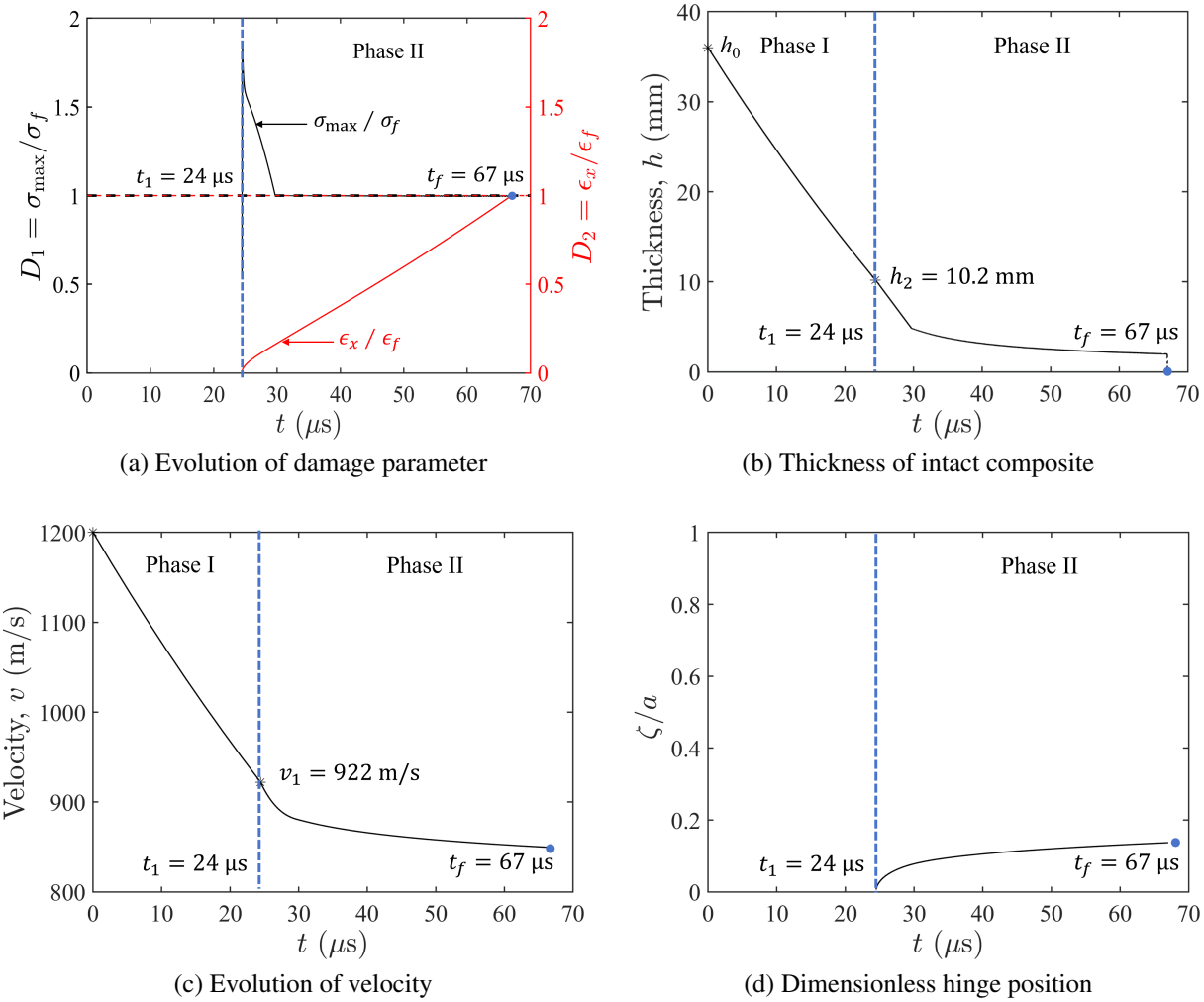

(a) Evolution of damage parameter

(b) Thickness of intact composite

(c) Evolution of velocity

(d) Dimensionless hinge position

Figure 13: Analytical predictions of the time-history of (a) damage parameters, (b) thickness of intact composite and (c) velocity and (d) dimensionless hinge position for a 36 mm thick laminated plate impacted by a blunt projectile of diameter $2R$ =12.7 mm at v_i =1200 m/s. Complete penetration occurs at the time instant of t_f = 67μs.

Fig. 13b. This is because, in the current analytical modelling, the tensile strain at the plate centre is identical for different sub-laminates since it was assumed that the deformation was unvaried through the thickness. Therefore, when the failure occurs at $D_2 = 1$, the damage criterion would be satisfied across all the sub-laminates. This prediction is reasonable since according to experimental observation in [11, 19] that the intact composite can be ruptured together by tensile tearing. Since the intact composite was penetrated continuously during phase II, the resistance force to arrest the projectile was minimal, leading to a significant residual velocity of v_r = 849 m/s. Due to the rather transient response, i.e. t_f=67 μs, the distance that the hinge travels is limited $\zeta(t = t_f)/a = 0.14$ as seen in Fig. 13d.

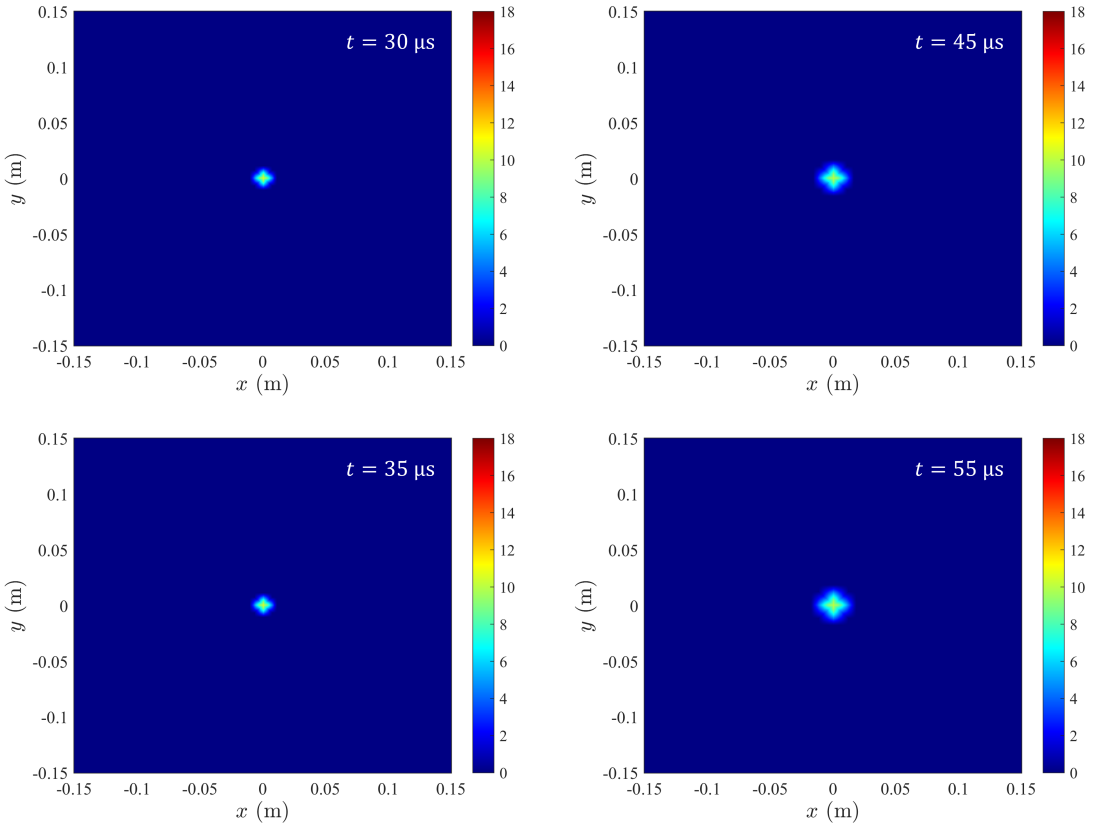

Figure 14: Analytically predicted equivalent stress contours (in GPa) on the impact-receiving layer of a 36 mm thick laminated plate impacted by a projectile of diameter $2R$ =12.7 mm at v_i =1200 m/s.

Figure 14 shows the equivalent stress distribution on the impact-receiving layer at selected time frames from $t = 25 - 65$ μs. The equivalent stress was concentrated at the impact zone during the entire ballistic response, which attributed to the progressive failure and reduction of thickness according to the stress-based damage criterion as seen previously in Fig. 13. The rather short distance travelled by the hinge leads to the stress concentration.

4.2. Travelling hinge

As alluded to in the introduction, various assumptions and theories were used in the literature [22, 27, 43] regarding the motion of the hinge in the analytical modelling of the dynamic response of UHMWPE laminates subjected to ballistic impact. In this subsection, the assumptions in the literature were scrutinised. In the experimental work by Nguyen et al. [17], hinge position and speed of UHWMPE composite with three different thicknesses ranging from $h_0 = 10-36$ mm were recorded which served as benchmarks to evaluate the efficacy of predictions based on different assumptions. Notice that in all three test cases studied in this subsection (which coincide to the same in Fig. 7), full penetration did not take place.

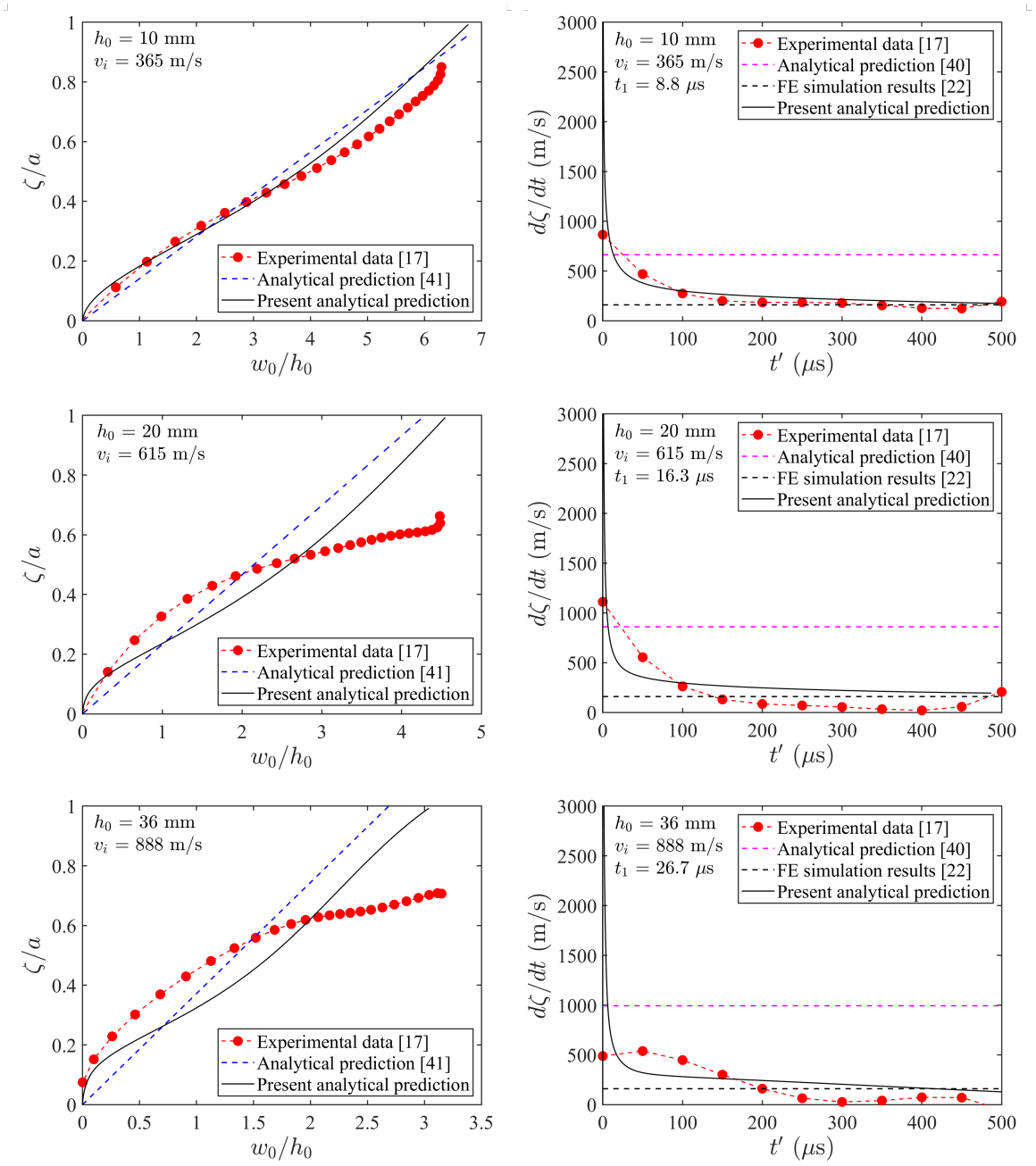

(a) Normalised deflection profile

(b) travelling hinge velocity (in m/s)

Figure 15: Comparison of experimental measurement to predictions by different models: (a) normalised deflection profiles and (b) hinge velocities. —●— by Nguyen et al. [17]; — by current analytical model; - - - by Leigh Phoenix and Porwal [42]; - - - by Smith et al. [43]; - - - by Yang et al. [22].

Figure 15a compares the normalised deflection profile (ζ/a as a function of w_0/h_0) obtained experimentally (extracted and re-arranged based on the experiment data of [17]) to the analytical predictions. Through a one-dimensional (1D) yarn impact model, Leigh Phoenix and Porwal [42] found that the deflection (or cone) angle γ is a constant value dependent only on the initial velocity of projectile v_i and the longitudinal wave velocity C_L, i.e.

$$\gamma \approx (2v_i/C_L)^{1/3}. \tag{26}$$

This approximation of deflection angle was employed recently in the analytical model by Zhang et al. [27]. Notice that $\tan\gamma$ is the slope of the blue dashed line in Fig. 15a. It can be seen that unlike the approximation made in [27, 42] where the slope is a constant, the dimensionless hinge position ζ/a increases nonlinearly with dimensionless deflection w_0/h_0 as seen in the experimental observation. The current analytical model successfully captured the nonlinear behaviour of the hinge position as a function of deformation. Both the current analytical prediction and the prediction based on Eq. 26 agree well with the experimental counterpart for the thin target (h_0 = 10 mm). However, for relatively thick targets (h_0 = 20 and 36 mm) where the 'pulling-in' effect was evident, both models led to overprediction of the hinge position for a given dimensionless TBD.

Figure 15b compares the time-history of hinge speed measured in the experiment of [17] to the predictions by different models (including the current analytical model, theoretical methods in [43] and finite element model in [22]). Smith [43] proposed that the travelling hinge velocity in isotropic one-dimensional elastic fibres is constant over time and can be expressed by:

$$\frac{d\zeta}{dt} = C_L\left[\sqrt{\epsilon_0\,(1+\epsilon_0)} - \epsilon_0\right] \tag{27}$$

where $\epsilon_0 \approx \left(\sqrt{2}v_i/C_L\right)^{4/3}$ is the 1D tensile strain. Notice that Smith's formula to estimate the travelling hinge speed was extensively used in the existing analytical work [30, 44]. On the other hand, Yang et al. [22] assumed a constant hinge velocity in their analytical model based on finite element simulation results for the same three tests in Fig. 15a. They found that travelling hinge velocity stabilises at a constant value of 165 m/s after an initial deceleration, which is regardless of the thickness of the UMHWPE laminated plate and the projectile velocity. The two horizontal lines refer to Eq. 27 and the constant value (165 m/s) used in the analytical model of [22]. It can be seen that hinge speed being a constant value was a crude assumption when comparing the horizontal lines to the experimental counterpart. The current analytical model captured qualitatively the significant drop in hinge speed with time. The hinge speed indeed reduces to a plateau value according to the experimental results. The predicted plateau value of the hinge speed agrees well with the numerical prediction by the sophisticated three-dimensional finite element model in [22], highlighting the accuracy of the current prediction on hinge speed. It is noteworthy that using detailed 3D finite element simulation to obtain value for the key variable defeats the purpose of quick analytical estimation.

4.3. The effect of increasing impact velocities

A finite number of analytical simulations were carried out to investigate the effect of initial velocities on the permanent hinge position, residual thickness and energy absorption characteristics of

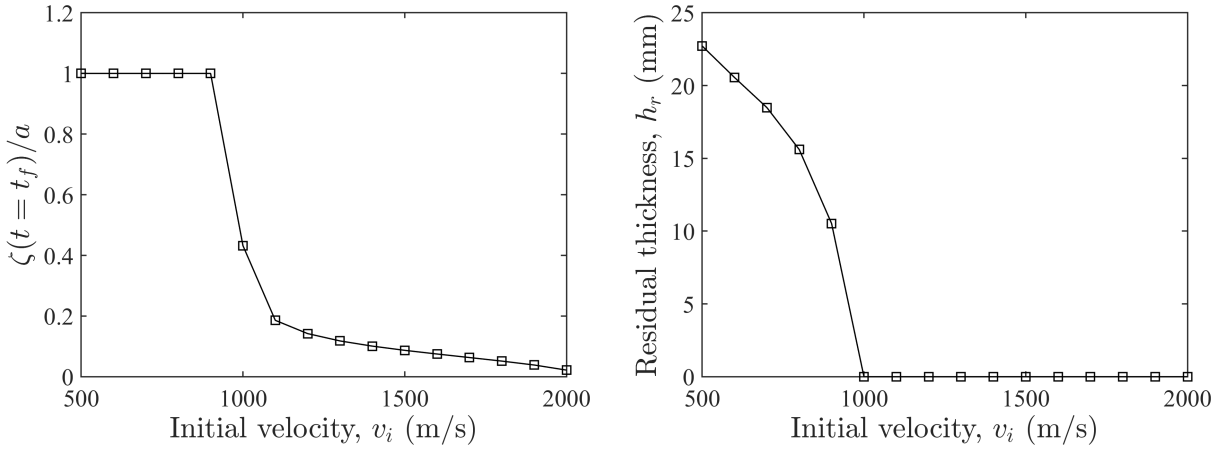

(a) Permanent dimensionless hinge position

(b) Residual thickness

Figure 16: Analytical predictions of (a) permanent dimensionless hinge position and (b) residual thickness of a 36 mm thick laminated plate impacted by a projectile of diameter $2R$ =20 mm at at different initial velocities.

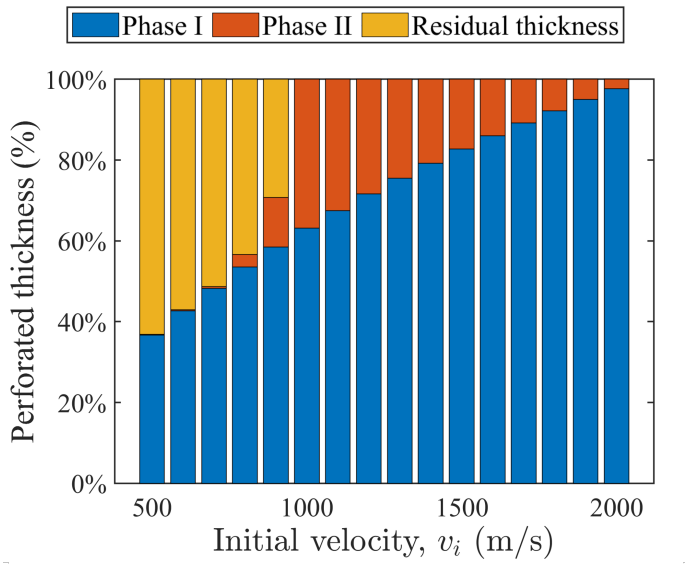

Figure 17: Proportion of penetration depth in phase I and phase II of a 36 mm thick laminated plate impacted by a projectile of diameter $2R$ =20 mm at at different initial velocities.

the UMHWPE laminated plate. The analytical predictions are shown in Figs. 16-18. The hinge can only reach the boundary at a low level of initial velocity as seen in Fig. 16a. The permanent hinge position reduces abruptly with increasing v_i after full penetration occurs. With a higher initial velocity, the residual thickness decreases monotonically, as seen in Fig. 16b. The proportions of penetration depths in phase I and II as well as the residual thickness were delineated in Fig. 17. It is increasing to note that phase I dominates the penetration depth regardless of the initial

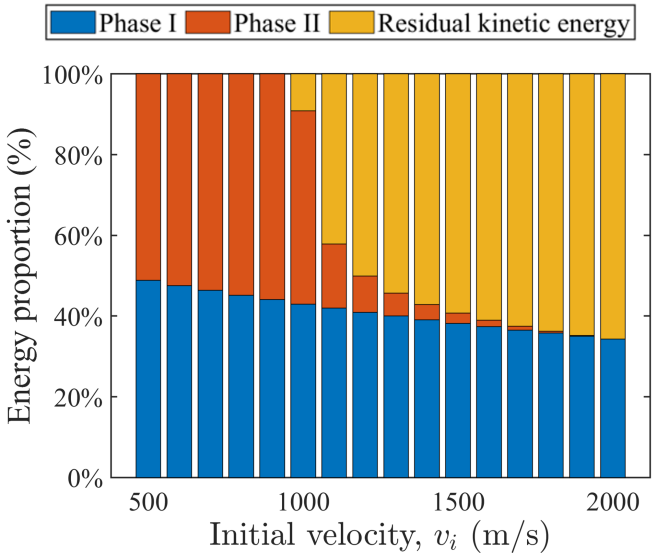

Figure 18: Partition of energy in phase I and II.

velocity. Progressive failure may not occur (zero perforated thickness in phase II) when the impact loading is not sufficiently intense. After full penetration occurs, perforated thickness reduces and increases in phase I and II respectively with increasing initial velocity.

Figure 18 presents the partitioning of energy in phase I and II as a function of initial velocity v_i. The proportion of energy absorbed during local penetration in phase I decreases slightly with higher initial impact velocity. Bulging deformation response in phase II plays a key role in dissipating the kinetic energy of the projectile at an initial velocity that is lower than the ballistic limit velocity. When full penetration occurs, the energy absorption during phase II quickly diminishes with greater v_i leading to a significant residual kinetic energy of the projectile.

5. Conclusion

An analytical model is developed and validated against existing experimental data, which is capable of predicting the transient bulging deflection and ballistic limit velocity of a fully clamped square UMHWPE laminated plate subjected to ballistic impact by a rigid blunt cylindrical projectile. The structural response of the UMHWPE laminated plate was separated into two uncoupled sequential phases: phase I is the local penetration into the laminated plate with negligible bulging deformation; phase II is the large bulging deformation with progressive failure through the thickness. Through the incorporation of an equivalent stress and a tensile strain criteria, the model can capture the progressive layer-by-layer failure in phase II. The travelling hinge is considered in the admissible velocity field within the modal analysis and is solved through the Lagrangian equation. Predictions by the analytical model are shown to be in reasonable agreement with existing experimental results. The following conclusions were made following our analysis:

- Equivalent stress was found to be maximum at the plate center which was initially concen-

trated at the impact zone before spreading to a larger region with the travelling hinge.

- Travelling hinge's velocity drops nonlinearly with time before reaching a plateau value.
- Increasing the initial velocity of the projectile beyond ballistic limit would lead to a reduction of permanent hinge position, a reduction of proportion of perforated thickness in phase II.
- Energy absorbed in phase I is significantly higher than that in phase II when full penetration occurs.

Acknowledgment

This research was financially supported by the National Science Foundation of China under Grant No. 12102049 and 12221002, and the Program for Innovative Research Team Project in NORINCO GROUP. The authors are grateful to the anonymous reviewers for their helpful comments.

References

[1] Wu, S., Sikdar, P., Bhat, G. S., Recent progress in developing ballistic and anti-impact materials: Nanotechnology and main approaches, Defence Technology 21 (2023) 33–61.

[2] Joshi, A., Mishra, A., Saxena, V. K., Impact response and energy absorption mechanisms of uhmwpe fabric and composites in ballistic applications: A comprehensive review, Composites Part A: Applied Science and Manufacturing 185 (2024) 108314.

[3] Zhu, Y., Song, Y., Wu, W., Niu, W., Fan, Z., Wen, Y., Xu, C., Xia, M., Ballistic impact wave and bulge profile propagation characteristics and blunt injury assessment of uhmwpe laminate composite, Journal of Materials Research and Technology (2024) In press.

[4] Vargas-Gonzalez, L. R., Gurganus, J. C., Hybridized composite architecture for mitigation of non-penetrating ballistic trauma, International Journal of Impact Engineering 86 (2015) 295–306.

[5] Cong, C., Zhu, W., Liu, J., Wei, X., A review on the analytical and numerical models for ballistic limit of fiber-reinforced composites, Composite Structures 345 (2024) 118392.

[6] Doddamani, S., Kulkarni, S. M., Joladarashi, S., T s, M. K., Gurjar, A. K., Analysis of light weight natural fiber composites against ballistic impact: A review, International Journal of Lightweight Materials and Manufacture 6 (3) (2023) 450–468.

[7] Yuan, Z., Wang, K., Qiu, J., Xu, Y., Chen, X., A numerical study on the mechanisms of dyneema® quasi-isotropic woven panels under ballistic impact, Composite Structures 236 (2020) 111855.

[8] Hazzard, M. K., Trask, R. S., Heisserer, U., Van Der Kamp, M., Hallett, S. R., Finite element modelling of dyneema® composites: From quasi-static rates to ballistic impact, Composites Part A: Applied Science and Manufacturing 115 (2018) 31–45.

[9] Gilson, L., Imad, A., Rabet, L., Coghe, F., On analysis of deformation and damage mechanisms of dyneema composite under ballistic impact, Composite Structures 253 (2020) 112791.

[10] Zhu, Y., Liu, K., Wen, Y., Cui, G., Niu, W., Wang, Y., Cao, Y., Xu, C., Experimental and numerical study on the ballistic performance of ultrahigh molecular weight polyethylene laminate, Polymer Composites 42 (10) (2021) 5168–5198.

[11] Cao, M., Zhou, D., Wang, Z., Chen, L., An experimental study of the penetration resistance of uhmwpe laminates with limited thickness, Thin-Walled Structures 196 (2024) 111438.

[12] O'Masta, M. R., Crayton, D. H., Deshpande, V. S., Wadley, H. N. G., Mechanisms of penetration in polyethylene reinforced cross-ply laminates, International Journal of Impact Engineering 86 (2015) 249–264.

[13] Ćwik, T. K., Iannucci, L., Curtis, P., Pope, D., Investigation of the ballistic performance of ultra high molecular weight polyethylene composite panels, Composite Structures 149 (2016) 197–212.

[14] Haris, A., Tan, V. B. C., Effects of spacing and ply blocking on the ballistic resistance of uhmwpe laminates, International Journal of Impact Engineering 151 (2021) 103824.
[15] He, Y., Jiao, Y., Zhou, J. Q., Lei, H., Jia, N., Chen, L., Zhang, D., Ballistic response of ultra-high molecular weight polyethylene laminate impacted by mild steel core projectiles, International Journal of Impact Engineering 169 (2022) 104338.
[16] Wang, H., Hazell, P. J., Shankar, K., Morozov, E. V., Escobedo, J. P., Impact behaviour of dyneema® fabric-reinforced composites with different resin matrices, Polymer Testing 61 (2017) 17–26.
[17] Nguyen, L. H., Lässig, T. R., Ryan, S., Riedel, W., Mouritz, A. P., Orifici, A. C., A methodology for hydrocode analysis of ultra-high molecular weight polyethylene composite under ballistic impact, Composites Part A: Applied Science and Manufacturing 84 (2016) 224–235.
[18] O'Masta, M. R., Deshpande, V. S., Wadley, H. N. G., Mechanisms of projectile penetration in dyneema encapsulated aluminum structures®, International Journal of Impact Engineering 74 (2014) 16–35.
[19] Karthikeyan, K., Russell, B. P., Polyethylene ballistic laminates: Failure mechanics and interface effect, Materials & Design 63 (2014) 115–125.
[20] Zhu, W., Huang, G., Feng, S., Stronge, W. J., Conical nosed projectile perforation of polyethylene reinforced cross-ply laminates: Effect of fiber lateral displacement, International Journal of Impact Engineering 118 (2018) 39–49.
[21] Schiffer, A., Cantwell, W. J., Tagarielli, V. L., An analytical model of the dynamic response of circular composite plates to high-velocity impact, International Journal of Impact Engineering 85 (2015) 67–82.
[22] Yang, S., Yan, Z., Gao, Y., Zhang, Y., Wang, Y., Liu, Z., Numerical and theoretical modeling of the elastic-plastic bulging deformation of uhmwpe composite laminate under high-speed impact, International Journal of Impact Engineering 182 (2023) 104771.
[23] Chocron, S., King, N., Bigger, R., Walker, J. D., Heisserer, U., van der Werff, H., Impacts and waves in dyneema® hb80 strips and laminates, Journal of Applied Mechanics 80 (031806).
[24] Zhu, Q., Yu, Z., A perturbation-based model for the prediction of responses involving delamination during small mass impacts on orthotropic composite plates, Composites Science and Technology 208 (2021) 108754.
[25] Zhang, T. G., Satapathy, S. S., Vargas-Gonzalez, L. R., Walsh, S. M., Ballistic impact response of ultra-high-molecular-weight polyethylene (uhmwpe), Composite Structures 133 (2015) 191–201.
[26] He, Y., Zhou, J. Q., Jiao, Y., Lei, H., Zhao, Z., Fang, D., Ballistic response mechanism and resistance-driven evaluation method of uhmwpe composite, Defence Technology (2024) In press.
[27] Zhang, R., Han, B., Zhou, Y., Qiang, L., Zhao, C., Zhao, Z., Zhang, Q., Ju, Y., Lu, T. J., Mechanism-driven analytical modelling of uhmwpe laminates under ballistic impact, International Journal of Mechanical Sciences 245 (2023) 108132.
[28] Liu, P., Wang, Z., Zhou, H., Zhang, H., Huang, G., An analytical model to predict back face deformation of hybrid soft body armors under ballistic impact, International Journal of Impact Engineering 180 (2023) 104723.
[29] Jintao, L., Moubin, L., An analytical model to predict the impact of a bullet on ultra-high molecular weight polyethylene composite laminates, Composite Structures 282 (2022) 115064.
[30] Langston, T., An analytical model for the ballistic performance of ultra-high molecular weight polyethylene composites, Composite Structures 179 (2017) 245–257.
[31] Yuan, Y., Zhu, L., Bai, X., Yu, T. X., Li, Y., Tan, P. J., Pressure–impulse diagrams for elastoplastic beams subjected to pulse-pressure loading, International Journal of Solids and Structures 160 (2019) 148–157.
[32] Yuan, Y., Xu, C., Xu, T., Sun, Y., Liu, B., Li, Y., An analytical model for deformation and damage of rectangular laminated glass under low-velocity impact, Composite Structures 176 (2017) 833–843.
[33] Yuan, Y., Tan, P. J., Li, Y., Dynamic structural response of laminated glass panels to blast loading, Composite Structures 182 (2017) 579–589.
[34] Nguyen, L. H., Ryan, S., Cimpoeru, S. J., Mouritz, A. P., Orifici, A. C., The effect of target thickness on the ballistic performance of ultra high molecular weight polyethylene composite, International Journal of Impact Engineering 75 (2015) 174–183.
[35] Yu, T. X., Chen, F. L., The large deflection dynamic plastic response of rectangular plates, International Journal of Impact Engineering 12 (4) (1992) 605–616.
[36] Hoo Fatt, M. S., Lin, C., Perforation of clamped, woven e-glass/polyester panels, Composites Part B: Engineer-

ing 35 (5) (2004) 359–378.
[37] Olsson, R., Impact response of orthotropic composite plates predicted from a one-parameter differential equation, AIAA Journal 30 (6) (1992) 1587–1596.
[38] Timoshenko, S., Woinowsky-Krieger, S., Theory of Plates and Shells, Engineering mechanics series, McGraw-Hill, 1959.
URL https://books.google.com/books?id=rTQFAAAAMAAJ
[39] Guo, G., Alam, S., Peel, L. D., An investigation of deformation and failure mechanisms of fiber-reinforced composites in layered composite armor, Composite Structures 281 (2022) 115125.
[40] Jones, N., Structural Impact, 2nd Edition, Cambridge University Press, New York, 2012.
[41] Liu, Y., Zhang, H., Huang, G., Zhou, H., Chen, J., Wang, Z., Theoretical model for predicting stabbing resistance of soft body armor comprising fibrous composites, International Journal of Impact Engineering 180 (2023) 104716.
[42] Leigh Phoenix, S., Porwal, P. K., A new membrane model for the ballistic impact response and v50 performance of multi-ply fibrous systems, International Journal of Solids and Structures 40 (24) (2003) 6723–6765.
[43] Smith, J. C., McCrackin, F. L., Schiefer, H. F., Stress-strain relationships in yarns subjected to rapid impact loading: Part v: Wave propagation in long textile yarns impacted transversely, Textile Research Journal 28 (4) (1958) 288–302.
[44] Mamivand, M., Liaghat, G. H., A model for ballistic impact on multi-layer fabric targets, International Journal of Impact Engineering 37 (7) (2010) 806–812.